

# Method for overcoming the finite space-bandwidth limitation of digital holograms in holography

BYUNG GYU CHAE

*Holographic Contents Research Laboratory, Electronics and Telecommunications Research Institute, 218 Gajeong-ro, Yuseong-gu, Daejeon 34129, Republic of Korea*  
[bgchae@etri.re.kr](mailto:bgchae@etri.re.kr)

## Abstract:

A digital hologram has a finite space-bandwidth, which determines the spatial resolution and angular field of view of its reconstructed image. However, higher space-bandwidth induces aliased replica patterns in the Fresnel diffraction. This study analyzes the spatial distribution of the angular spectrum in an undersampled hologram using angle modulation in the complex domain. The replica functions are identified as phase-modulated functions by multiples of the sampling frequency, with the spatial frequency range extending continuously from the original function into the regions of the replica functions. Simulations of optical imaging confirm the theoretical predictions, demonstrating that imaging performance beyond the space-bandwidth limitation of a digital hologram is achievable. Specifically, a method is proposed to address the challenge of limited viewing angles in holographic displays. This approach provides an alternative solution to overcome the constraints imposed by the finite space-bandwidth of digital holograms.

© 2024 Optica Publishing Group

## 1. Introduction

The holographic image is reconstructed either numerically or optically from the digital hologram. A digital hologram has a finite space-bandwidth, which determines key imaging performance metrics such as the resolution limit and angular field of view [1,2]. The space-bandwidth  $B_w$  of the Fresnel hologram sampled at  $\Delta$  pixel interval with  $N \times N$  pixels is represented as

$$B_w = \frac{N\Delta}{\lambda z}. \quad (1)$$

According to the Abbe diffraction theory, the resolution limit  $R_{\text{lim}}$  of the reconstructed image is given as the reciprocal of this value,  $R_{\text{lim}} = \frac{\lambda z}{N\Delta} = \frac{\lambda}{2 \sin \theta}$  [3–6]. In optical reconstruction, the viewing angle is twice the angle value  $\theta$ . The hologram aperture constrains the ability to capture the spatial frequency components of the diffractive wave.

Aliased replica patterns are formed when the required bandwidth exceeds the bandwidth supported by the hologram's pixel [7–10]. Spatial frequency components higher than the Nyquist frequency are aliased, making them appear as lower frequency components of the original function. The spatial frequency  $f$  increases linearly along the spatial direction, and the aliased frequency  $f_a$  is determined by the relationship [11]:

$$f_a = |f - n f_s|, \quad (2)$$

where  $f_s$  is the sampling frequency and  $n$  is an integer. This property results in the formation of replica functions that are spatially distributed at regular periodic intervals. Figure 1 illustrates the aliasing phenomenon for a point-source hologram sampled at a lower sampling rate. The complex-valued hologram  $h(x, y)$  for a point object  $\delta(x, y)$  is expressed as the impulse response

function,  $h(x, y) = \frac{e^{ikz}}{i\lambda z} \exp \left[ \frac{i\pi}{\lambda z} (x^2 + y^2) \right]$ . Using the modulated form of the Fourier-transformed function, the sampled hologram at an interval  $\Delta x$  along the  $x$ -axis is written as follows [12, 13]:

$$\sum_n h(n\Delta x) \delta(x - n\Delta x) = \frac{1}{\Delta x} \sum_n c_n h \left( x + \frac{\lambda z n}{\Delta x} \right). \quad (3)$$

For simplicity, a one-dimensional description is used hereafter. The replication pattern are formed at a reduced period of  $\frac{\lambda z}{s\Delta x}$  when undersampled by a factor  $s$  of  $\Delta x$ . Continuous response functions are obtained through the inverse Fourier transform of modulated angular spectra. The angular spectra, within the range of the original function, are folded at intervals determined by the folding frequency.

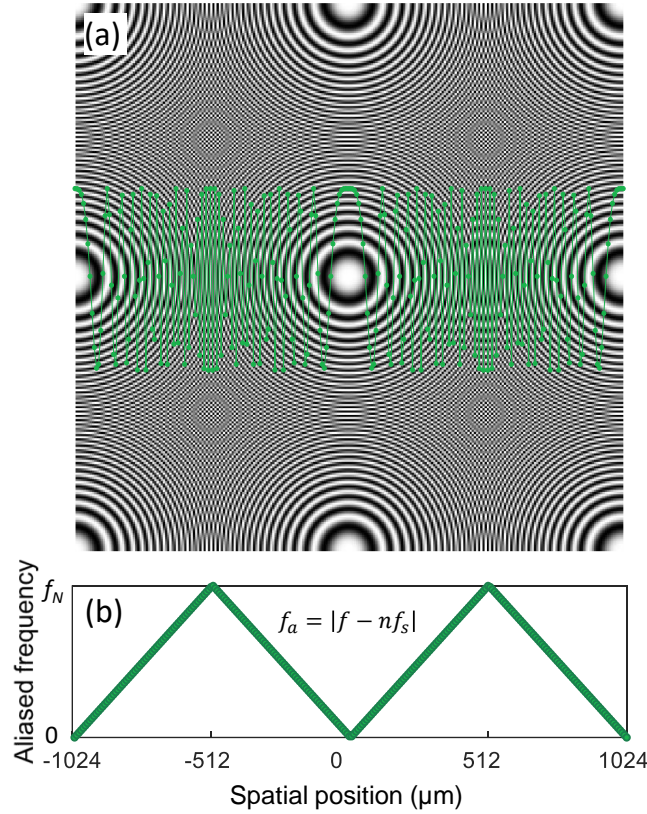


Fig. 1. Aliasing phenomenon for a point-source hologram sampled at a lower sampling rate. (a) The real-valued hologram made at a distance of a half of  $z_c$  exhibits four replica Fresnel zones. The inset graph is the 1D quadratic phase function along the lateral distance at the center. (b) Aliased frequencies for the quadratic phase function.

Previously, it was reported that this type of hologram reconstructs a holographic image with a space-bandwidth that spans the entire aperture of the digital hologram, regardless of aliased fringes [13–15]. This suggests that the replica functions correspond to the high spatial-frequency components of the hologram field. However, the above description of aliasing makes it difficult to explain numerical and experimental results. The space-bandwidth remains confined to the original function due to replication, meaning that the diffraction performance is limited to its initial value. As a result, establishing a unified understanding in this field has proven challenging to date.

In this study, an angular spectrum in the undersampled hologram with aliased replica fringes is investigated using angle modulation in the complex plane. The replica functions exhibit a phase modulation pattern created by a carrier wave that corresponds to multiples of the sampling frequency. The spatial frequency increases linearly across the region of the replica functions. The replica function plays a role in the higher frequency components of original function, as well as additive replication. Sampling condition in the numerical calculation of the Fresnel field is observed by applying this analysis to optical kernel functions. Numerical simulation of optical imaging reveals a consistency of this scheme, and especially, an approach to recover the smaller viewing angle in holographic display is proposed.

## 2. Angular spectrum distribution in the undersampled hologram

### 2.1. Spatial frequency in complex plane

The spatial frequency in the Fresnel hologram is represented as  $\frac{x}{\lambda z}$  from the quadratic phase term, which depends linearly on the lateral spatial distance. The distribution of spatial frequency in the undersampled hologram of a point source is investigated, particularly in the complex plane. The complex-valued hologram, consisting of  $256 \times 256$  pixels with a  $8\text{-}\mu\text{m}$  pixel pitch, was synthesized using the Fresnel diffraction formula with a single Fourier transform [14]. A unit-amplitude plane wave with a wavelength  $\lambda$  of  $532\text{ nm}$  was used. The hologram of a point object placed at a distance of a half of  $z_c$  results in the formation of four replica Fresnel zones, as shown in Fig 1(a). The critical distance  $z_c$  is the minimum distance at which hologram functions are free from replication effects:

$$z_c = \frac{N\Delta x^2}{\lambda}, \quad (4)$$

where the replication interval  $\frac{\lambda z}{\Delta x}$  in Eq. (3) equals the field extent  $N\Delta x$ . No aliased fringes appear for distances above  $z_c$ . For this configuration,  $z_c$  is calculated to be  $30.8\text{ mm}$ .

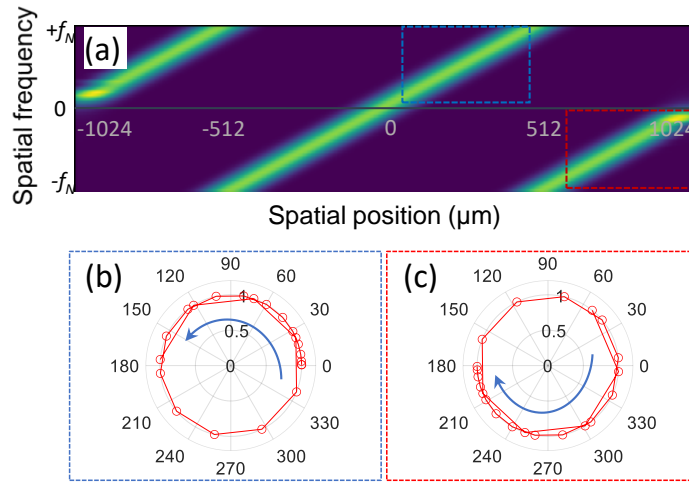


Fig. 2. Spatial frequency distribution of an undersampled point-source hologram in the complex domain. (a) Spatial frequency variation along the lateral spatial position. The trajectories of the position vectors (b) in the blue box and (c) in the red box, corresponding to those in Fig. 2(a), are plotted in polar coordinates, respectively.

Figure 2 illustrates the change in spatial frequency along the lateral distance. The spatial frequency along the  $x$ -axis at the center of the hologram is obtained using a commercial spectrum

calculation program, in Fig. 2(a). Unlike the aliased frequencies in the real domain, both negative and positive spatial frequency components appear in the complex plane. In the complex-valued function, the position vector with negative frequencies rotates clockwise, while the position vector with positive frequencies rotates counterclockwise.

The spatial frequency exhibits a linear dependence on the lateral spatial distance. On the positive-axis side, the spatial frequency increases continuously up to the Nyquist frequency, i.e.,  $f_N = 1.25 \times 10^5 \text{m}^{-1}$ . The position of the Nyquist frequency is estimated to be  $x = 512 \mu\text{m}$  using Eq. (1). At this point, the spatial frequency changes discontinuously to the negative Nyquist value, then continues to increase toward zero. The trajectories of the position vectors in these two distinct regions are plotted in polar coordinate, as depicted in Figs. 2(b) and 2(c). The position vector rotates from a counterclockwise direction to a clockwise direction at the Nyquist frequency. Similarly, the negative side shows symmetrical behavior.

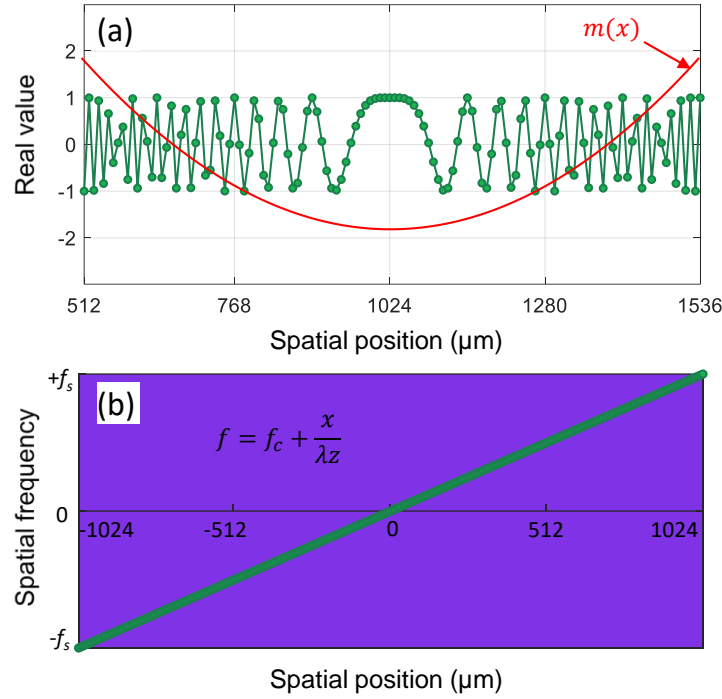


Fig. 3. Spatial frequency distribution after considering modulation form by a carrier wave. (a) The phase profile of the carrier wave modulated by the message signal at the +1<sup>st</sup>-order shifted position. The message signal is inserted at an arbitrary position. (b) The spatial frequency as a function of spatial position.

## 2.2. Angle modulation in the undersampled hologram

The spatial frequency distribution in an undersampled hologram can be interpreted using angle modulation in the complex plane. The shifted replica function in Eq. (3) is described as a phase-modulated function by a carrier wave:

$$c_n h \left( x + \frac{\lambda z n}{\Delta x} \right) = \exp \left[ i 2 \pi \left( \frac{n x}{2 \Delta x} + \frac{x^2}{2 \lambda z} \right) \right]. \quad (5)$$

In the phase modulation [11], the instantaneous phase  $\phi(x)$  is given by

$$\phi(x) = 2\pi f_c x + D_o m(x), \quad (6)$$

where the carrier wave is a sinusoidal wave with a carrier frequency,  $f_c = n \left( \frac{1}{\Delta x} \right)$ , expressed as  $e^{\frac{-in\pi x}{\Delta x}}$ , and the modulation index  $D_o$  is equal to one.

The message signal  $m(x)$  in the above equation is a simple quadratic function:

$$m(x) = \frac{\pi x^2}{\lambda z}. \quad (7)$$

The phase of the carrier wave is modulated by the message signal, leading to the formation of a replica zone, which appears as moire fringes shifted to  $\frac{\lambda z n}{\Delta x}$ . Figure 3(a) shows the +1<sup>st</sup>-order replica function shifted to a position of 1024  $\mu\text{m}$ . Since the amplitude of the phase-modulated wave remains constant, the average power of the spatially distributed wave is one half.

The instantaneous frequency in phase modulation is calculated from the derivative of phase value:

$$f = \frac{1}{2\pi} \frac{d\phi(x)}{dx} = f_c + D_o \frac{dm(x)}{dx} = f_c + \frac{x}{\lambda z}. \quad (8)$$

The spatial frequency  $f$  is the sum of the original frequency  $\frac{x}{\lambda z}$  and the carrier frequency. Here, the carrier frequency is a multiple of the sampling frequency. Figure 3(b) draws the angular spectrum distribution considering the modulation behaviour. The spatial frequency on both sides of the  $x$ -axis increases from zero to the sampling frequency of  $f_s = 2.5 \times 10^5 \text{m}^{-1}$  without any discontinuity.

Likewise, all shifted replica functions can be expressed as higher spatial-frequency components corresponding to those of the original function. This analysis in the complex plane demonstrates that the shifted replica function represents not only aliased fringes but also higher spectral components. Although the description focuses on the central function, it applies equally to the replica functions. It is interesting because the spatial frequency is relative depending on the criteria. Consequently, the spatial-frequency components of each function should be still the high-frequency components of adjacent functions.

### 3. Imaging behaviour of undersampled hologram

#### 3.1. Sampling condition in numerical simulation

To observe the propagation behavior of the diffracted wave  $g(x', y')$  from the undersampled hologram  $h(x, y)$  to a far distance, it is essential to first investigate the sampling properties. The sampling condition in a digitized space is well established using the Fresnel diffraction formula [10, 16–18]:

$$g(x', y') = \frac{ie^{-ikz}}{\lambda z} \exp \left[ -i \frac{\pi}{\lambda z} (x'^2 + y'^2) \right] \mathbf{FT} \left[ h(x, y) \exp \left[ -i \frac{\pi}{\lambda z} (x^2 + y^2) \right] \right]. \quad (9)$$

The quadratic phase term within the Fourier transform ( $\mathbf{FT}$ ) determines the sampling criterion, as the hologram's spatial frequency does not depend on a distance. To avoid aliasing, the sampling rate  $f_s$  must exceed twice the maximum spatial frequency  $f_{x,\max}$  of the phase term:

$$f_s \geq 2f_{x,\max} = \frac{2x_{\max}}{\lambda z}. \quad (10)$$

Using a sampling rate of  $\frac{1}{\Delta x}$  and the hologram's field size,  $N\Delta x = 2|x_{\max}|$ , the well-sampling condition with respect to the reconstruction distance is given by

$$z \geq \frac{N\Delta x^2}{\lambda}. \quad (11)$$

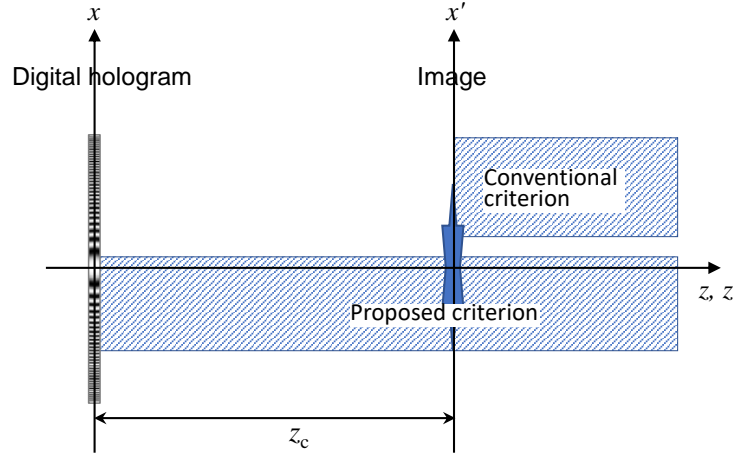


Fig. 4. Proper sampling conditions in numerical simulation of the Fresnel diffraction waves. Numerical calculations conserving higher spatial-frequency components can be performed at all propagation distances.

According to Eq. (11), proper sampling is achievable only at distances greater than the critical distance, as illustrated in Fig. 4. Below this critical distance, aliasing error occurs. The phenomenon of aliasing can be understood by analyzing the undersampling properties of a quadratic phase exponential within the Fourier transform. At a distance  $z_l$  shorter than the critical distance, the quadratic phase function becomes undersampled, leading to the formation of replica functions. These replicas are directly associated with the generation of high-order diffraction terms.

However, the replica functions preserve the same higher spatial frequencies as the original function. Before the undersampling process, the original function comprises  $N_o$  pixels with a pixel pitch of  $\Delta x_o$ . The maximum spatial frequency remains conserved, ensuring that the Nyquist sampling criterion is satisfied:

$$z_l \geq \frac{N_o \Delta x_o^2}{\lambda}. \quad (12)$$

Thus, while aliasing-induced high-order diffractions occur, numerical calculations that retain higher spatial-frequency components are feasible at all propagation distances.

### 3.2. Optical simulations

Figure 5 illustrates the imaging behavior for the undersampled hologram. The diffractive wave  $g(x', y')$ , propagating from the hologram function  $h(x, y)$ , was numerically calculated by using the Rayleigh-Sommerfeld diffraction formula [1]:

$$g(x', y') = \frac{i}{\lambda} \iint E_R(x, y) h(x, y) \frac{\exp(-ikr)}{r} dx dy, \quad (13)$$

where an incident plane wave with a unit amplitude,  $E_R(x, y)$  is assumed, and  $k$  is the wavenumber of  $2\pi/\lambda$ . The intensity of the diffractive waves along the lateral line at the center is displayed as a function of the propagating distance,  $r = \sqrt{z^2 + (x' - x)^2 + (y' - y)^2}$ . The well-behaved waves propagate at all propagation distances without disturbance. The point image is focused in the Fresnel diffraction region, and aliased replica functions generate corresponding replica images.

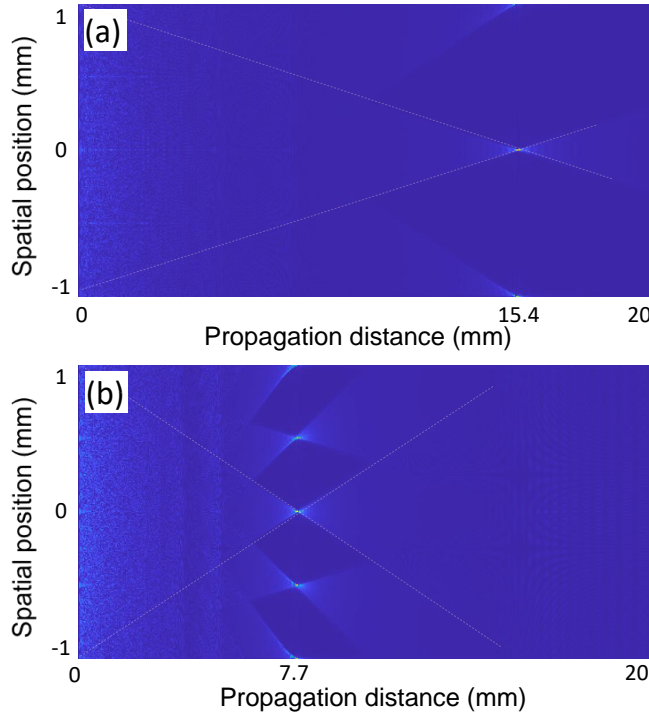


Fig. 5. Imaging behavior of an undersampled point-source hologram simulated using the Rayleigh-Sommerfeld diffraction formula. (a) Propagating waves from the hologram prepared using a point object placed at half- $z_c$ . (b) Propagating waves from the hologram prepared using a point object placed at quarter- $z_c$ . The intensity of the diffractive waves along the  $x$ -axis is displayed. The aspect ratio of the image is conveniently adjusted. Inset lines are included to clearly indicate the diffraction angle,  $2\theta$ .

The sampled hologram produces high-order diffraction terms that propagate in specific directions. Individual diffraction waves cannot be distinguished in the region close to the hologram.

As shown in Fig. 5(a), the point image is formed at a half of  $z_c$ , i.e., 15.4 mm, and then spreads out as it propagates further. The image resolution of  $4 \mu\text{m}$  is twice as high as the hologram pixel size, and similarly, the spreading angle is double that of the diffraction angle of hologram pixel. The spreading angle is estimated to be approximately  $7.6^\circ$ , whereas the diffraction angle for a hologram pixel size of  $8 \mu\text{m}$  is  $3.8^\circ$ . The hologram made at a quarter of critical distance reconstructs the point image with a spatial resolution of  $2 \mu\text{m}$ , where the spreading angle, i.e., the viewing angle increases to  $15.2^\circ$ , in Fig. 5(b). Both the image resolution and spreading angle increase as the synthesis distance of the digital hologram decreases. It appears that the entire aperture of the digital hologram contributes to image formation, regardless of aliasing.

Meanwhile, to clarify this property, the high-order diffractions of the replica functions are distinguished through numerical simulation. Figure 6 is the schematic diagram showing the multiple diffractions from the undersampled hologram. The reconstruction behavior from a hologram made at one-third of  $z_c$  is drawn for the sake of convenience. Replica functions generate high-order diffractions, forming replicas of the point image arranged at uniform intervals in the image plane. The Fresnel zone of replica function corresponding to the  $+1^{\text{st}}$ -order image contributes to the formation of both the original image and the  $-1^{\text{st}}$ -order image. In this scenario, it is difficult to determine whether the enhanced spatial resolution arises from the extended high-spectrum components of the replica functions.



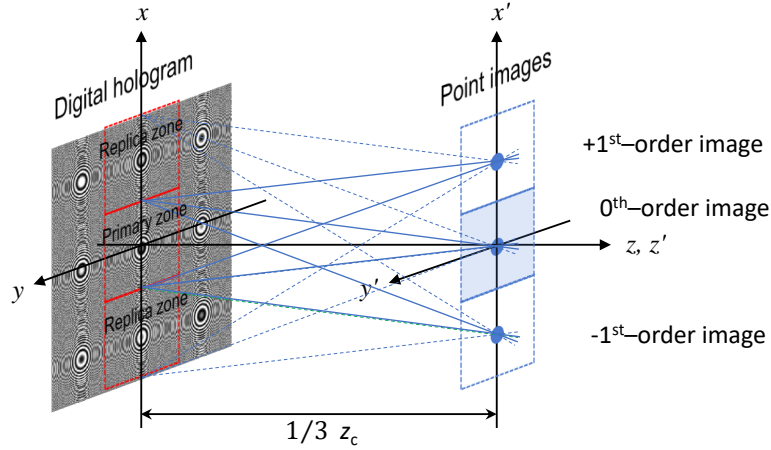


Fig. 6. Schematic diagram illustrating multiple diffractions from an undersampled hologram. Point-image reconstruction is described using a hologram made at one-third of  $z_c$ . For clarity, multiple diffractions for three Fresnel zones in the central region are drawn.

The angular spectrum method allows the image space to be confined within the diffraction zone of a hologram pixel, effectively eliminating interference from high-order diffractions during numerical calculations. The algorithm involves a double Fourier transform [1, 6]:

$$g(x', y') = \mathbf{IFT} \left( \mathbf{FT} [E_R(x, y)h(x, y)] \exp [i\pi\lambda z(f_x^2 + f_y^2)] \right), \quad (14)$$

where  $\mathbf{IFT}$  indicate the inverse Fourier transform. The pixel resolutions in each space are governed by the sampling relation:

$$\Delta x' = \frac{1}{N\Delta f} = \Delta x. \quad (15)$$

The pixel values in both hologram and image planes are the same via the pixel value  $\Delta f$  in the intermediate Fourier plane. Only the zeroth-order region in the intermediate plane,  $N\Delta f$  is utilized, thereby excluding high-frequency components beyond the diffraction limit.

The sampling condition can be determined through an analysis of the embedded transfer function. The transfer function in the Fourier space is a quadratic phase exponential, allowing the sampling rule used for the response function in the real space to be applied here as well. As a result, numerical calculations conserving higher spatial-frequency components through above formula can be performed at all propagation distances.

Figure 7(a) presents the simulated diffractive waves obtained using the angular spectrum method. The high-order diffractions are removed due to an upper bound frequency of  $1.25 \times 10^5 \text{ m}^{-1}$ , effectively functioning as a low-pass filter. The point image is formed from the primary zone which occupies half the width of the hologram aperture. The spatial resolution of the point image is  $8 \mu\text{m}$ , based on Eqs. (1) and (15). The spreading angle of the propagating wave is estimated to be  $3.9^\circ$ .

The diffraction behavior of a two-fold upsampled hologram was investigated. The upsampling process increases the pixel resolution from  $256 \times 256$  pixels at  $8 \mu\text{m}$  to  $512 \times 512$  pixels at  $4 \mu\text{m}$  by simply duplicating the pixel values of the original undersampled hologram. As depicted in Fig. 7(b), each pixel in the original hologram corresponds to four identical pixels in the two-fold upsampled version. In this circumstance, while the two-fold upsampled hologram retains the



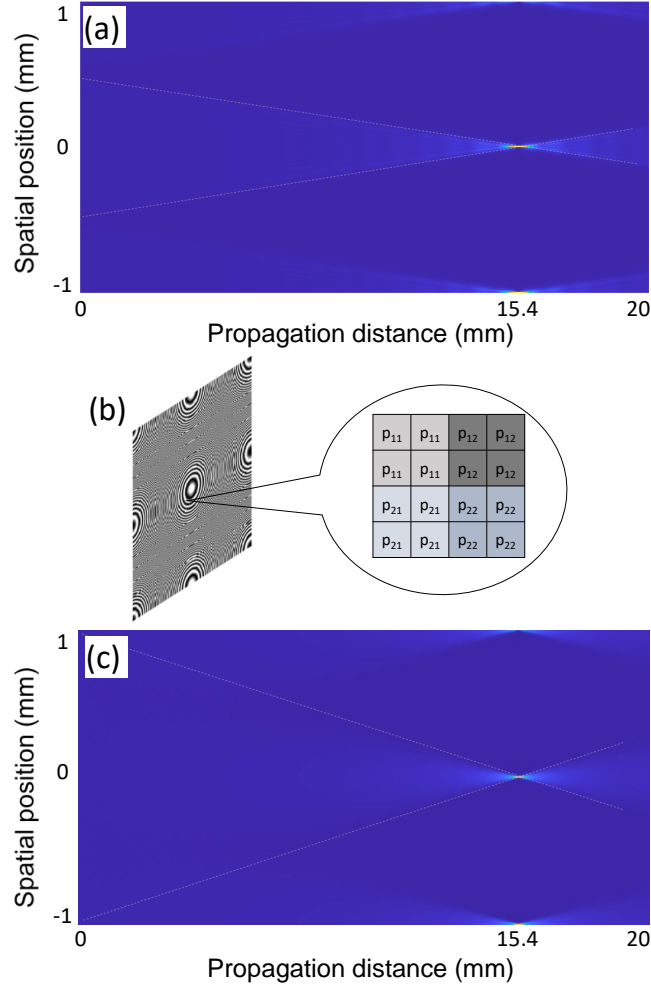


Fig. 7. Simulated propagating waves using the angular spectrum method. (a) High-order diffractions are eliminated and the point image is formed from the primary zone. (b) The upsampling process is performed by duplicating the pixel values of the original undersampled hologram. (c) The diffraction behavior of the two-fold upsampled hologram is illustrated.

replica patterns, the calculation process is performed in the two-fold enhanced Fourier space, based on Eq. (15). There is no confinement by the upper bound frequency.

Previously, we reported that this type of upsampling process effectively suppresses high-order diffractive waves [13]. The two-fold upsampling process restrains the  $\pm 1^{\text{st}}$ -order images. The propagating behavior in Fig. 7(c) demonstrates an absence of interference from multiple diffractions caused by replica functions. Irrespective of high-order terms by neighbouring replica functions, the central point image is formed through the entire region of the digital hologram. The diffracted wave converges at an angle of  $7.2^\circ$  before focusing on the point image, achieving a spatial resolution of  $4 \mu\text{m}$ .

This behavior clearly shows that the spatial frequency continuously increases across the shifted replica functions. Therefore, even the maximum spatial frequency in the undersampled hologram is defined by the entire aperture of the hologram in Eq. (1). Numerical simulation well matches with the theoretical description. The spatial resolution and viewing angle of the restored image

are not fixed from the diffraction angle by a hologram pixel. It is apparent that these values vary depending on the focal distance in a digital hologram with finite space-bandwidth, in Fig. 8. Previously, it was reported that the viewing angle changes according to this relationship, as demonstrated in optical experiments [13].

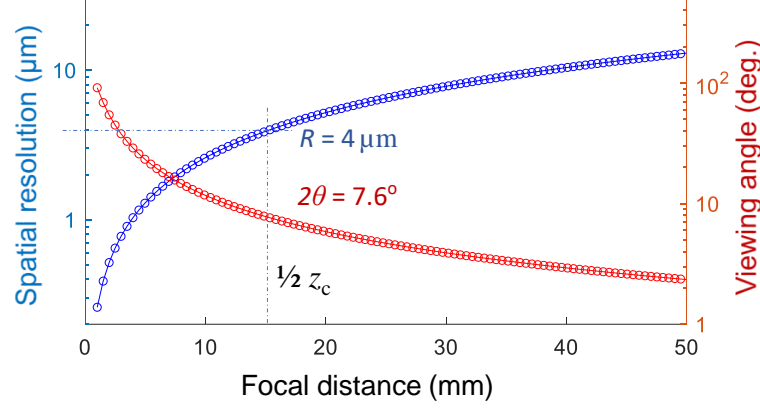


Fig. 8. Spatial resolution and viewing angle of the restored image as a function of focal distance. The inset line indicates the values for the focused image at a distance of a half of  $z_c$ .

#### 4. Discussions

The imaging performance depends on the space-bandwidth product of the digital hologram. A digitized device with a large space-bandwidth product is essential for acquiring high-resolution images at a large scale. Since the hologram undersampled by a low-resolution pixel includes components of higher spatial frequencies, a high-resolution and large-scale image can be obtained using a digitized device with finite bandwidth, provided that methods are developed to eliminate additive noise, such as replica patterns and high-order diffractions.

In holographic displays, the limited viewing angle remains a significant bottleneck for commercializing three-dimensional displays [19–22]. A 3D image is reconstructed by illuminating the pixelated modulator loading the digital hologram with a coherent plane wave. Commercial modulators can typically achieve only a few degrees of viewing angle at best. However, by leveraging the angular spectrum distribution properties of undersampled holograms, even commercial modulators can achieve a sufficiently large viewing angle. Previously, we explored a method to extend the viewing angle beyond the diffraction limit in a commercial spatial light modulator. This study further clarifies the proposed process, which primarily consists of two steps: First, an optimization algorithm is developed to suppress the formation of replica patterns in the undersampled hologram [14]. Second, an upsampling process is applied to eliminate high-order diffractions. This is achieved by attaching a fine-definition grid to the pixelated modulator [13].

The expansion of the spatial-frequency distribution into the undersampled regions can also be applied to the Rayleigh-Sommerfeld region. The optical kernel function used in this regime takes the form,  $\exp\left(i2\pi z\sqrt{\frac{1}{\lambda^2} - f_x^2 - f_y^2}\right)$ , where the replica patterns may appear distorted. Moreover, it remains uncertain whether this approach is applicable to the evanescent field region. If these two issues can be theoretically resolved, this strategy could pave the way for meaningful advancements in super-resolution imaging.

## 5. Conclusions

A mathematical description of the angular spectrum distribution demonstrates that an under-sampled hologram at a lower sampling rate can reconstruct an image with the same spatial resolution and angular field of view as a properly sampled hologram. The spatial frequencies are found to be continuously distributed across the aliased replica functions. Moreover, the undersampled replica functions differ from the meaningless noise typically associated with conventional aliasing. Instead, they generate high-order diffractive waves that form replica images in the image plane. When these replica terms are effectively removed through suitable external operations, high-performance imaging can be achieved, surpassing the inherent space-bandwidth limitations of a digital hologram. One practical example of this concept addresses the issue of limited viewing angles in holographic displays. This technology provides an alternative approach to overcome the finite space-bandwidth constraints of digital holograms, paving the way for enhanced imaging performance.

**Funding.** This work was supported by Institute for Information & Communications Technology Promotion (IITP) grant funded by the Korea government (MSIP) (2021-0-00745)

**Disclosures.** The authors declare no conflicts of interest.

## References

1. J. W. Goodman, *Introduction to Fourier Optics* (McGraw-Hill, 1996).
2. A. W. Lohmann, R. G. Dorsch, D. Mendlovic, Z. Zalevsky, and C. Ferreira, "Space-bandwidth product of optical signals and systems," *J. Opt. Soc. Am. A* **13**, 470-473 (1996).
3. P. Picart and J. Leval, "General theoretical formulation of image formation in digital Fresnel holography," *J. Opt. Soc. Am. A* **25**(7), 1744-1761 (2008).
4. D. P. Kelly, B. M. Hennelly, N. Pandey, T. J. Naughton, and W. T. Rhodes, "Resolution limits in practical digital holographic systems," *Opt. Eng.* **48**(9), 95801 (2009).
5. T. Latychevskaia and H.-W. Fink, "Inverted Gabor holography principle for tailoring arbitrary shaped three-dimensional beams," *Sci. Rep.* **6**, 26312 (2016).
6. B. G. Chae, "Analysis on angular field of view of holographic image dependent on hologram numerical aperture in holographic display," *Opt. Eng.* **59**(3), 035103 (2020).
7. T. M. Kreis, "Frequency analysis of digital holography," *Opt. Eng.* **41**(4), 771-778 (2002).
8. L. Onural, "Sampling of the diffraction field," *Appl. Opt.* **39**(32), 5929-5935 (2000).
9. A. Stern and B. Javidi, "Analysis of practical sampling and reconstruction from Fresnel fields," *Opt. Eng.* **43**(1), 239-250 (2004).
10. B. G. Chae, "Analysis on image recovery for on-axis digital Fresnel hologram with aliased fringe generated from self-similarity of point spread function," *Opt. Commun.* **466**, 125609 (2020).
11. A. V. Oppenheim, A. S. Willsky, and S. H. Nawab, *Signals and Systems* (Prentice-Hall, 2010).
12. L. Onural, "Some mathematical properties of the uniformly sampled quadratic phase function and associated issues in Fresnel diffraction simulations," *Opt. Eng.* **43**(11), 2557-2563 (2004).
13. B. G. Chae, "Wide viewing-angle holographic display based on enhanced-NA Fresnel hologram," *Opt. Express* **29**(23), 38221-38236 (2021).
14. B. G. Chae, "Viewing-angle expansion in holographic displays implemented with a modulator having finite space-bandwidth," *Opt. Express* **31**(23), 37900-37910 (2023).
15. B. G. Chae, "Spatial resolution enhancement in holographic imaging via angular spectrum expansion," *Opt. Continuum* **3**(3), 263-277 (2024).
16. D. Mas, J. Garcia, C. Ferreira, L. M. Bernardo, and F. Marinho, "Fast algorithms for free-space diffraction patterns calculations," *Opt. Commun.* **164**, 233-245 (1999).
17. D. G. Voelz and M. C. Roggemann, "Digital simulation of scalar optical diffraction: revisiting chirp function sampling criteria and consequences," *Appl. Opt.* **48**(32), 6132-6142 (2009).
18. J.-P. Liu, "Controlling the aliasing by zero-padding in the digital calculation of the scalar diffraction," *J. Opt. Soc. Am. A* **29**(9), 1956-1964 (2012).
19. T. Kozacki, M. Kujawińska, G. Finke, B. Hennelly, and N. Pandey, "Extended viewing angle holographic display system with tilted SLMs in a circular configuration," *Appl. Opt.* **51**(11), 1771-1780 (2012).
20. K. Yamamoto, Y. Ichihashi, T. Senoh, R. Oi, and T. Kurita, "3D objects enlargement technique using an optical system and multiple SLMs for electronic holography," *Opt. Express* **20**(19), 21137-21144 (2012).
21. Y. Takaki and S. Uchida, "Table screen 360-degree three-dimensional display using a small array of high-speed projectors," *Opt. Express* **20**(8), 8848-8861 (2012).
22. M. Gopakumar, J. Kim, S. Choi, Y. Peng, and G. Wetzstein, "Unfiltered holography: optimizing high diffraction orders without optical filtering for compact holographic displays," *Opt. Lett.* **46**(23), 5822-5825 (2021).